PHYSICAL REVIEW B **96**, 161113(R) (2017)

Confinement and fermion doubling problem in Dirac-like Hamiltonians

B. Messias de Resende, F. Crasto de Lima, R. H. Miwa, E. Vernek, and G. J. Ferreira
Instituto de Física, Universidade Federal de Uberlândia, Uberlândia, MG 38400-902, Brazil
(Received 10 August 2017; published 25 October 2017)

We investigate the interplay between confinement and the fermion doubling problem in Dirac-like Hamiltonians. Individually, both features are well known. First, simple electrostatic gates do not confine electrons due to the Klein tunneling. Second, a typical lattice discretization of the first-order derivative $k \to -i\partial_x$ skips the central point and allow spurious low-energy, highly oscillating solutions known as fermion doublers. While a no-go theorem states that the doublers cannot be eliminated without artificially breaking a symmetry, here we show that the symmetry broken by the Wilson's mass approach is equivalent to the enforcement of hard-wall boundary conditions, thus making the no-go theorem irrelevant when confinement is foreseen. We illustrate our arguments by calculating the following: (i) the band structure and transport properties across thin films of the topological insulator Bi_2Se_3, for which we use *ab initio* density functional theory calculations to justify the model; and (ii) the band structure of zigzag graphene nanoribbons.

DOI: 10.1103/PhysRevB.96.161113

Topological insulators (TIs) constitute a class of materials that exhibit the ubiquitous property of being an insulator in their bulk, while presenting metallic states on their edges or surfaces [1–4]. The key ingredient for the underlying physics of the TIs is a strong spin-orbit interaction, which generically leads to a Dirac-like spectrum. At low energy, the effective Hamiltonians for the edge/surface states are linear in the momentum, yielding a massless Dirac spectrum. The resulting helical band structure is topologically protected against backscattering, thus providing perfect conducting channels that are potentially useful for future electronic devices [5,6], quantum computation [7], and optical applications [8].

The numerical approach to investigate the properties (e.g., transport, dynamics, confinement) [9–11] of these systems often requires a lattice discretization of the Hamiltonian. Unfortunately, standard finite difference descriptions of the first-order derivatives of linear in momentum $\hbar k$ Hamiltonians are infected by the fermion doubling problem (FDP). This yields spurious low-energy states, as exemplified in Fig. 1(a). Even though the energy dispersion is well described by the discrete Hamiltonian at small k, the doublers appearing for large k will affect the transport and dynamics of the system. There are many ways to eliminate the doublers [12,13], e.g., staggered fermions [14–17], Wilson's mass [18–21], nonlocal discretizations [22–24], and extra artificial dimensions [25–28]. Each of them presents its own advantages and disadvantages. There is, however, a common and seemingly unsolvable problem: As required by the Nielsen-Ninomiya theorem (NNT) [29,30], all these approaches introduce a symmetry breaking or nonlocality.

The k-linear models also display the Klein tunneling "paradox" [31,32], which states that simple electrostatic barriers are transparent and cannot confine massless electrons. This is a consequence of the constant Fermi velocity of the linear dispersion, which allows perfect matching of the injected and transmitted waves. Consequently, to attain confinement, one needs to either open a gap by breaking a symmetry in the outer region [21,33–38], or invoke finite-size effects [39].

In this Rapid Communication we ask whether it is possible to eliminate the FDP in a finite system by breaking the same symmetry that provides the confinement. The answer is yes. The short argument is as follows: Since the symmetry is already broken by the confinement, there is no harm in introducing a Wilson's mass that breaks the same symmetry. More interestingly, here we show that the Wilson's mass not only eliminates the doublers, but also defines the type of hard-wall confinement that is imposed by vanishing boundary conditions. To present this argument, we start with a simple unidimensional model that captures its essence. Here, we solve the linear Hamiltonian with vanishing flux hard-wall boundaries [35,37], and compare it with the solutions obtained by introducing a parabolic Wilson's mass term $\propto wk^2$ and vanishing wave-function hard-wall boundaries. We find that the solutions match for a small, but finite, Wilson's mass w, while for $w \to 0$, one recovers the spurious doublers.

Next, we discuss the surface states of the three-dimensional (3D) topological insulator Bi_2Se_3 as a prototype model to illustrate our findings. Here, we consider two different forms of the Wilson's mass term to show that it can either break time-reversal symmetry (TRS), as in Refs. [21,37,38], or a sublattice

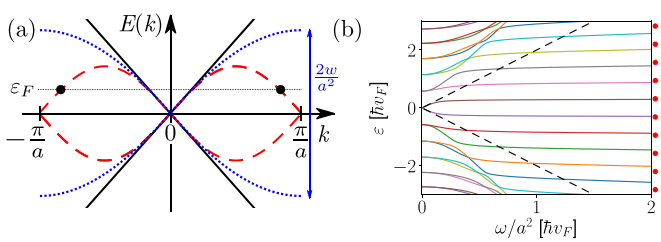

FIG. 1. (a) In a discrete lattice with spacing a, the linear dispersion $\varepsilon = \pm\hbar v_F k$ of the continuous model (solid black line) is replaced by $\varepsilon = \pm\hbar v_F (2a)^{-1} \sin(ka)$ (dashed red line), yielding the "doublers" at the Fermi energy ε_F (black dots). A finite Wilson's mass term $\propto wk^2$ eliminates the doublers by opening a gap at $k = \pm\pi/a$ (dotted blue line). (b) Quantized energies of the linear spectrum due to hard-wall confinement as a function of the Wilson mass w. The numerical solutions (solid lines) approach the exact solutions (red dots) in the range $|\varepsilon| < 2w/a^2$ (black dashed lines). For $w \to 0$, the numerical solutions merge to form the doublers.

chiral symmetry. Its consequences for the energy levels and degeneracies of a quantum dot, and the transport properties across a ribbon are discussed. We use a modified version of the effective Hamiltonian for the Bi_2Se_3 from Refs. [40,41] fitted to first-principles calculations from the VASP code [42,43]. The effective model is then implemented numerically using the KWANT code [44]. Additionally, we briefly present the case of zigzag graphene nanoribbons, which is a challenging case for effective models [17].

Fermion doubling. To establish our arguments, let us first consider a simple one-dimensional Dirac-like model given by the Hamiltonian $H_\xi = \hbar v_F \mathcal{M}_\xi k$, where v_F is the Fermi velocity, k is the momentum along a generic coordinate ξ, and $\mathcal{M}_\xi$ is a unitary Hermitian matrix. The exact energy spectrum of H_ξ is $\varepsilon = \pm\hbar v_F k$, which is the Dirac cone illustrated in Fig. 1(a). However, if one desires to find the spectrum numerically via finite differences, the momentum $\hbar k = -i\hbar\partial_\xi$ takes a discrete form. To keep H Hermitian, one typically chooses the symmetric finite difference approach, leading to an expression that skips the central point, i.e., $\partial_\xi \psi(\xi_j) \approx [\psi(\xi_{j+1}) - \psi(\xi_{j-1})]/2a$, where the integer j labels the points in the discrete lattice of spacing a. Consequently, it allows for low-energy, highly oscillating states of a topological origin [29,30], thus yielding the doublers shown in Fig. 1(a).

Wilson's mass. Here, we choose the Wilson's mass approach [18–21] to eliminate the doublers. The idea is to introduce a parabolic correction $H_W = w\mathcal{M}_c k^2$ to $H_\xi \to H_\xi + H_W$. For small k, the linear terms dominate and H_W does not significantly affect the band structure. However, this term eliminates the doublers as its discretization couples all three points j, and $j \pm 1$, thus opening a gap $2w/a^2$ at $k = \pm\pi/a$, as shown in Fig. 1(a). The penalty for using H_W is that it breaks a chiral symmetry of the linear H_ξ. Next, we argue that this penalty is irrelevant if one chooses $\mathcal{M}_c$ to be the same unitary matrix that the defines the hard-wall confinement.

Hard-wall boundary conditions. The hard-wall boundary condition for H_ξ (without H_W) is imposed by the limit $\alpha \to \infty$ of the confining potential $H_C = \alpha\mathcal{M}_c\Theta(|\xi| - \xi_0)$, where $\Theta(\xi)$ is the Heaviside step function defining the walls at $\xi = \pm\xi_0$. The unitary matrix $\mathcal{M}_c$ must break a symmetry of H_ξ to open a gap 2α in the outer region ($|\xi| > \xi_0$). At the interface, the spinor is discontinuous [33,34], and integrating $H_\xi\psi = \varepsilon\psi$ across the interface we obtain the boundary condition [35,37]

$$(\pm i\mathcal{M}_\xi + \mathcal{M}_c)\psi(\xi_0) = 0, \tag{1}$$

where the matrices $(\pm i\mathcal{M}_\xi + \mathcal{M}_c)$ are singular, thus allowing nontrivial solutions. Notice that we have used the same matrix $\mathcal{M}_c$ to define here this boundary condition for linear H_ξ, and above to introduce the Wilson's mass parabolic term H_W. This assures that both approaches will break the same symmetry of H_ξ.

In contrast to Eq. (1), the Wilson's mass model $H_\xi + H_W$ allows trivial vanishing boundary conditions $\psi(\pm\xi_0) = 0$. Therefore, now we have two different approaches to apply a hard-wall confinement. Moreover, our choice of a simple H_ξ allows for analytical solutions (up to a transcendental equation) for the boundary condition from Eq. (1), thus avoiding the discretization and the FDP all together. In Fig. 1(b) we compare these solutions with a numerical finite difference model for $H_\xi + H_W$ with vanishing boundary conditions as a function of the Wilson's mass w. For $w \to 0$, pairs of eigenstates merge to form the degenerate doublers, but are split for finite w. An appropriate value for w can be chosen such that the energy window of interest lies within the Wilson's mass gap $2w/a^2$ [see Fig. 1(a)], and preserves the dominance of the linear term over the parabolic correction, which yields $\frac{1}{2}a^2|\varepsilon| < w < (\hbar v_F)^2/|\varepsilon|$ [43].

Bi_2Se_3 *thin films.* Next, we apply our approach to model thin films of the topological insulator Bi_2Se_3. Bulk Bi_2Se_3 is composed of van der Waals interacting quintuple layers (QLs). Each QL is formed by an alternation of covalent bonded hexagonal monolayers of Se-Bi-Se-Bi-Se. The effective Hamiltonian for both the bulk and its surface states are well known [37,40,41]. Here, we choose to write it on the basis of surface states of semi-infinite solutions from the top (T) and bottom (B) surfaces, i.e., $\{\varphi_{T\uparrow}(\boldsymbol{r}),\varphi_{T\downarrow}(\boldsymbol{r}),\varphi_{B\uparrow}(\boldsymbol{r}),\varphi_{B\downarrow}(\boldsymbol{r})\}$, where $\{\uparrow,\downarrow\}$ refers to the spin along z. Up to linear order in $\boldsymbol{k} = (k_x,k_y)$ the Hamiltonian reads [43]

$$H = \varepsilon_0 + \hbar v_F(k_x\gamma_{3y} - k_y\gamma_{3x}) + F\gamma_{30} + \Delta\gamma_{10} + B\gamma_{0z}, \tag{2}$$

where $\gamma_{ij} = \tau_i \otimes \sigma_j$, $\boldsymbol{\sigma}$ and $\boldsymbol{\tau}$ are $\mathfrak{su}(2)$ operators acting on spin and surface subspaces, ε_0 is the energy reference, F represents the intensity of a structural inversion asymmetry (SIA) field, Δ is the hybridization coupling between the surfaces, and B is a generic Zeeman field. We extract these parameters from DFT simulations [43,45]. For a pristine Bi_2Se_3 stacking of seven QLs, the Dirac bands are well defined and we find $v_F = 479$ nm/ps [46], $\varepsilon_0 = -12$ meV, $F = \Delta \approx 0$. Additionally, in the Supplemental Material we analyze the band structure of Bi_2Se_3 contacted by a Ti metallic lead. At this interface, a charge transfer yields a bias field $F \approx 95$ meV and a shift of the Dirac cones $\varepsilon_0 \approx -150$ meV. Moreover, these are coupled to metallic bands near the Fermi level, which will allow us to use the wide-band approximation later on.

A finite F splits the Dirac cones from the top and bottom surfaces without opening a gap, while Δ opens a gap hybridizing the surfaces, and B opens a gap by breaking TRS. Therefore, there are two possible Wilson mass terms that can be added to H to eliminate the doublers and define the types of hard-wall boundary conditions. These are

$$H_B = m_B\frac{a^2}{4}k^2\gamma_{0z} \quad \text{and} \quad H_\Delta = m_\Delta\frac{a^2}{4}k^2\gamma_{10}. \tag{3}$$

Hereafter we will refer to m_B and m_Δ as the Wilson masses for a B-type and Δ-type hard-wall confinements. These break the same symmetries as B and Δ. Similarly to the range of w above, the appropriate range for $m_{B/\Delta}$ is $|\varepsilon|/2 < |m_{B/\Delta}| < (2\hbar v_F/a)^2/|\varepsilon|$ [43].

Chiral symmetries. A chiral symmetry [47–49] is defined by an operator $\mathcal{P}$ that anticommutes with H. Consequently, it assures that for every eigenstate of H with energy ε, there is a chiral partner with energy $-\varepsilon$. For the Bi_2Se_3 H above, we find four candidate operators for chiral symmetries that obey

$$\{\mathcal{P}_{0z}, H - \varepsilon_0\} = 2B + 2\Delta\gamma_{1z} + 2F\gamma_{3z}, \tag{4}$$

$$\{\mathcal{P}_{10}, H - \varepsilon_0\} = 2B\gamma_{1z} + 2\Delta, \tag{5}$$

$$\{\mathcal{P}_{20}, H - \varepsilon_0\} = 2B\gamma_{2z}, \tag{6}$$

$$\{\mathcal{P}_{3z}, H - \varepsilon_0\} = 2B\gamma_{30} + 2F\gamma_{0z}, \tag{7}$$

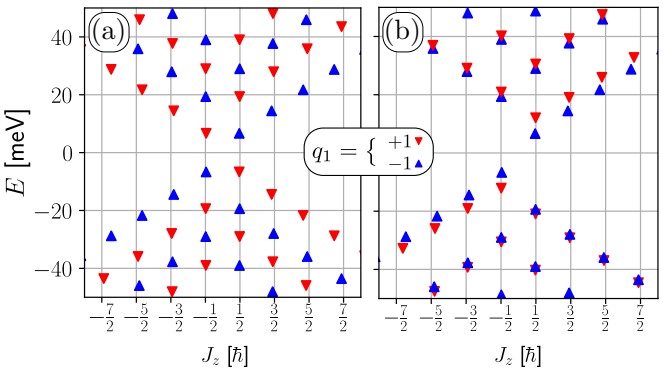

FIG. 2. Spectrum of a circular Bi_2Se_3 thin-film quantum dot as a function of the total angular momentum j_z. The up- (blue) and down-pointing (red) triangles refer to the chiral charge $q_{1z} = \pm 1$. (a) For the Δ-type confinement both the chirality ($\varepsilon_{j_z,-q_{1z}} = -\varepsilon_{j_z,q_{1z}}$) and TRS ($\varepsilon_{-j_z,-q_{1z}} = \varepsilon_{j_z,q_{1z}}$) are preserved. (b) The B-type confinement breaks both chiral and TRS, but preserves their product ($\varepsilon_{-j_z,q_{1z}} = -\varepsilon_{j_z,q_{1z}}$).

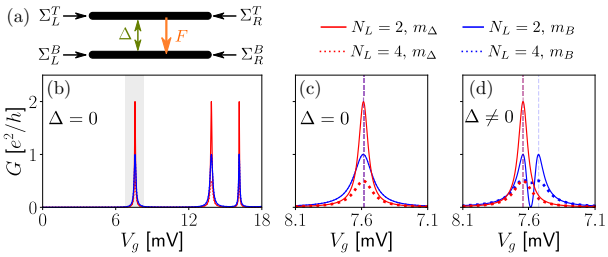

FIG. 3. (a) Illustration of the top and bottom Bi_2Se_3 surfaces coupled by Δ, biased by F, and contacted by effective leads introduced by the self-energies Σ_ℓ^j. (b) Conductance vs V_g for $\Delta = 0$. The $V_g \sim 7.6$ mV peak is shown in detail in (c) for $\Delta = 0$, and (d) for $\Delta = 0.1$ meV. Red (blue) lines correspond to Δ-type (B-type) confinement, and solid (dashed) lines refer to the $N_L = 2$ (4) terminal model.

where $\mathcal{P}_{ij} \equiv \gamma_{ij}$. For simplicity, we omit the Wilson masses m_B and m_Δ, but their contributions follow the B and Δ terms above. In accordance with the NNT [29], [30], a finite m_B or m_Δ breaks some chiral symmetries. Particularly, $m_B \neq 0$ breaks them all. However, we find that combining the $\mathcal{P}$ operators above with the TRS operator $\mathcal{T} = -i\gamma_{0y}\mathcal{K}$ ($\mathcal{K}$ is complex conjugation) as $\mathcal{P}'_j = \mathcal{P}_j\mathcal{T}$, one obtains similar anticommutation relations independent of B [43].

Circular dot. To illustrate the Δ- and B-type confining potentials and the chiral symmetries, we consider a circular quantum dot of radius R on a Bi_2Se_3 thin film modeled by H in Eq. (2) and the Wilson masses in Eq. (3). For this geometry, the z-component $J_z = L_z + S_z$ of the total angular momentum is conserved [37], which allows us to label the states by its eigenvalues $j_z = (m + \frac{1}{2})\hbar$, where m is an integer. The discrete spectrum of this quantum dot for Δ-type ($m_\Delta = -500$ meV) and B-type ($m_B = -500$ meV) confining potentials are shown in Fig. 2 as a function of j_z. For simplicity, in both cases, $\varepsilon_0 = F = B = 0$, $\Delta = -5$ meV, and $v_F = 479$ nm/ps. The eigenvalues are obtained using a square lattice in which the sites are connected only for $r \leqslant R = 50$ nm, and $N = 100$ sites along the diagonal.

For the Δ-type confinement shown in Fig. 2(a), $\mathcal{P}_{20}$ and $\mathcal{P}_{3z}$ are chiral symmetries. These combine to define the chiral charge $\mathcal{Q}_{1z} = -i\mathcal{P}_{20}\mathcal{P}_{3z} = \gamma_{1z}$, such that $[\mathcal{Q}_{1z}, H] = 0$. Together with j_z, the eigenvalues $q_{1z} = \pm 1$ of $\mathcal{Q}_{1z}$ are used to label the eigenenergies as $\varepsilon_{n,j_z,q_{1z}}$, where n is an extra index that labels the different solutions with the same j_z and q_{1z}. Since $\{\mathcal{P}, H\} = 0$, $[\mathcal{P}, J_z] = 0$ and $\{\mathcal{P}_j, \mathcal{Q}_{1z}\} = 0$, every state with energy $\varepsilon_{n,j_z,q_{1z}}$ has a chiral partner with energy $\varepsilon_{n,j_z,-q_{1z}} = -\varepsilon_{n,j_z,q_{1z}}$. Similarly, the TRS produces the Kramer partners with energies $\varepsilon_{n,-j_z,-q_{1z}} = \varepsilon_{n,j_z,q_{1z}}$. Combined, these two symmetries produce the X-shaped spectrum of Fig. 2(a). In contrast, Fig. 2(b) shows the spectrum for the B-type confinement, for which the chiral symmetries $\mathcal{P}$ and TRS are broken. Here, the time-reversal chiralities $\mathcal{P}'_{20}$ and $\mathcal{P}'_{3z}$ are preserved. These combine to give the same chiral charge $\mathcal{Q}_{1z}$. However, now $\{\mathcal{P}', J_z\} = 0$ and $[\mathcal{P}', \mathcal{Q}_{1z}] = 0$. Consequently, a state with energy $\varepsilon_{n,j_z,q_{1z}}$ has a time-reversal chiral partner with energy $\varepsilon_{n,-j_z,q_{1z}} = -\varepsilon_{n,j_z,q_{1z}}$, yielding the single linear branch and the shifted bands in Fig. 2(b). The agreement between these exact relations and the numerical results in Fig. 2 show that our approach does eliminate the doublers without any harm to the chiralities that remain in the presence of confinement.

Conductance across a ribbon device. As another example of our main result, let us now calculate the conductance across the Bi_2Se_3 surface. We consider a geometry that was recently realized experimentally [50], where the leads are contacted with metal electrodes, while the scattering region is pristine Bi_2Se_3. The conductance peaks reflect the degeneracy of the states, which are directly affected by the symmetry breaking discussed previously. In the leads, the hybridization between the topmost QLs Bi_2Se_3 and the metal [51] puts the chemical potential within an energy window composed of Bi_2Se_3 surface and Ti states [43]. Therefore, we can judiciously assume that the effect of the leads is essentially to broaden the discrete Fabry-Perot resonances in the confined central region. Within this simplified description, we introduce the self-energies $\Sigma_\ell^j(E)$ with $\ell = L, R$ (for left and right) and $j = T, B$ (for top and bottom), which in the wide-band limit are $\Sigma_\ell^j(E) = -i\bar{\Sigma}_\ell^j(E_F)\Theta(D - |E - E_F|)$; see Fig. 3(a). Here, $\bar{\Sigma}_\ell^j(E_F)$ is a real quantity giving the broadening of the sites interfacing the ℓth TI lead, and D is some suitable cutoff energy. This rather crude simplification is very suitable for numerical simulations of realistically sizable systems. Nonetheless, it gives qualitatively plausible results for the conductance as compared to those obtained with a complete model.

For the scattering region we consider square surfaces of pristine Bi_2Se_3 of side $W = 100$ nm, discretized into a 20×20 site grid. A two-terminal case ($N_L = 2$) is built with the top left and right ($\ell = L$ and R) leads with symmetric broadening $\bar{\Sigma}_\ell^T = 1$ meV. Moreover, despite the reduced coupling to the metal contact, a four-terminal ($N_L = 4$) case is also considered with $\bar{\Sigma}_\ell^B = 1$ meV. Figure 3(b) shows the conductance G versus gate voltage V_g for $\Delta = 0$, $N_L = 2(4)$ as solid (dashed) lines, and both Δ-type (blue lines, $m_\Delta = -100$ meV) and B-type (red lines, $m_B = -100$ meV) confinements. Figures 3(c) and 3(d) zoom to show details of the $V_g \sim 7.6$ mV peaks. For the $N_L = 2$ case with the

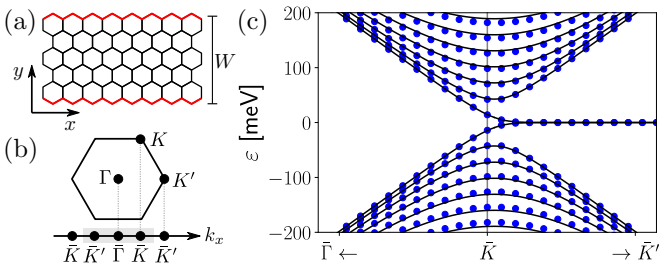

FIG. 4. (a) A graphene nanoribbon with zigzag terminations and width W. (b) The first Brillouin zone of bulk graphene and its projection (shaded area) along the nanoribbon's k_x. (c) Band structure around $\bar{K}$ for a $W \approx 71$ nm ribbon comparing the analytical solution (black solid lines) and our numerical approach with a Wilson mass (blue dots).

Δ-type confinement, we observe that the peaks reach $2G_0$, where the factor 2 results from the TR pair of degenerate states (symmetric and antisymmetric combinations of the top and bottom surface states) that contribute as independent conducting channels. These peaks are not substantially affected by the presence of small $\Delta \neq 0$, as we see in Fig. 3(d). In contrast, for the B-type confinement the conductance peaks reach only G_0 in Fig. 3, for $\Delta = 0$. Indeed, here TRS is broken and one would already expect a single conducting channel. More interestingly, a finite $\Delta = 0.1$ meV splits this peak, showing $G = 0$ in the middle. This can be understood in terms of the $\mathcal{P}'$ chiral symmetries and the conserved chiral charge $\mathcal{Q}_1$, which assures that for $\Delta = 0$, every state located in one surface has a degenerate partner in the other surface [43]. A finite Δ couples these partners, producing two coherent channels that interfere destructively ($G = 0$) for some particular value of V_g. For $N_L = 4$, the conductance is still calculated between the top terminals (dashed lines in Fig. 3). Overall, this yields a decrease of G whenever the top and bottom surfaces are coupled (Δ-type confinement or $\Delta \neq 0$). In this situation, the channels involving the bottom surface states are broadened by the bottom contacts, therefore they act as incoherent channels, destroying the perfect inference.

Zigzag graphene nanoribbon. As a final application of our proposal, we present the band structure of a zigzag graphene nanoribbon around its K point in Fig. 4. This is a particularly interesting case as it allows us to compare the numerical results directly with well-known analytical solutions [52–55], which are shown as black solid lines in Fig. 4(c). For the numerical approach we start with graphene's effective model around K, $H_K = \hbar v_F \boldsymbol{\sigma} \cdot (\boldsymbol{k} - \boldsymbol{K})$, where $\boldsymbol{k}$ is measured from the origin at $\bar{\Gamma}$ in Fig. 4(b), and $k_y \to -i\partial_y$ is discretized into $N = 100$ sites. Around K', one obtains $H_{K'}$ replacing $\sigma_y \to -\sigma_y$ and $\boldsymbol{K} \to \boldsymbol{K}'$, which compose our block-diagonal $H_0 = H_K \oplus H_{K'}$. To regularize the boundary conditions for the zigzag nanoribbon we consider a Wilson mass term $H_Z = m_z \frac{a^2}{4} k_y^2 (\tau_x \otimes \sigma_y)$, where τ_x couples the K and K' subspaces, and m_z is chosen within the range set by the inequalities discussed previously. The agreement between the numerical band structure and the exact solution shown in Fig. 4(c) is patent, which illustrates the effectiveness of our approach.

Conclusions. We have shown that the Wilson mass not only eliminates the doublers in Dirac-like Hamiltonians, but also allows us to control the hard-wall boundary conditions. This contrasts with the high-energy physics, where neither the broken symmetry nor confinement are desirable. Therefore, for confined solid state systems, the NNT is easily bypassed. Interestingly, these effects were overlooked in models that already include the parabolic terms [11,21,56,57]. Indeed, in the Bernevig-Hughes-Zhang (BHZ) model [56], for instance, the term $-Bk^2\sigma_z$ plays the role of the Wilson mass, with the Pauli matrix σ_z acting on the E_1/H_1 subspace, yielding a Dirac mass-type hard wall [57]. In contrast, graphene models are usually restricted to the linear terms, which limits its use. Here, we have seen that a zigzag termination can be well modeled by incorporating an appropriate Wilson's mass. For the armchair case, one can directly combine Ref. [35] with our approach.

Applying our model to model Bi_2Se_3 quantum dots, we have shown that numerical results satisfy all symmetry constraints that are compatible with the chosen type of confinement. Particularly, the Δ-type confinement is compatible with thin films [11], yielding noninteracting conductance peaks $G = 2\,e^2/h$, which is a necessary ingredient for the Kondo regime suggested in Ref. [50]. As a final remark, notice that Ref. [21] considers only a B-type mass, which breaks TRS, and the confinement properties are not discussed. Therefore, our model generalizes and improves their results.

Acknowledgments. The authors acknowledge the financial support from the Brazilian Agencies CNPq, CAPES, and FAPEMIG.

[1] B. A. Bernevig and S.-C. Zhang, Phys. Rev. Lett. **96**, 106802 (2006).
[2] M. König, S. Wiedmann, C. Brüne, A. Roth, H. Buhmann, L. W. Molenkamp, X.-L. Qi, and S.-C. Zhang, Science **318**, 766 (2007).
[3] M. Z. Hasan and C. L. Kane, Rev. Mod. Phys. **82**, 3045 (2010).
[4] X.-L. Qi and S.-C. Zhang, Rev. Mod. Phys. **83**, 1057 (2011).
[5] M. Götte, T. Paananen, G. Reiss, and T. Dahm, Phys. Rev. Appl. **2**, 054010 (2014).
[6] M. Götte, M. Joppe, and T. Dahm, Sci. Rep. **6**, 36070 (2016).
[7] H. P. Paudel and M. N. Leuenberger, Phys. Rev. B **88**, 085316 (2013).
[8] A. L. Yeats, Y. Pan, A. Richardella, P. J. Mintun, N. Samarth, and D. D. Awschalom, Sci. Adv. **1**, e1500640 (2015).
[9] Y. S. Kim, M. Brahlek, N. Bansal, E. Edrey, G. A. Kapilevich, K. Iida, M. Tanimura, Y. Horibe, S.-W. Cheong, and S. Oh, Phys. Rev. B **84**, 073109 (2011).
[10] S. K. Mishra, S. Satpathy, and O. Jepsen, J. Phys.: Condens. Matter **9**, 461 (1997).
[11] L. Hao, P. Thalmeier, and T. K. Lee, Phys. Rev. B **84**, 235303 (2011).

[12] T. DeGrand, Eur. Phys. J. Spec. Top. **152**, 1 (2007).
[13] S. Chandrasekharan and U.-J. Wiese, Prog. Part. Nucl. Phys. **53**, 373 (2004).
[14] L. Susskind, Phys. Rev. D **16**, 3031 (1977).
[15] R. Stacey, Phys. Rev. D **26**, 468 (1982).
[16] J. Tworzydło, C. W. Groth, and C. W. J. Beenakker, Phys. Rev. B **78**, 235438 (2008).
[17] A. R. Hernández and C. H. Lewenkopf, Phys. Rev. B **86**, 155439 (2012).
[18] K. G. Wilson, Phys. Rev. D **10**, 2445 (1974).
[19] J. B. Kogut and L. Susskind, Phys. Rev. D **11**, 395 (1975).
[20] A. Bermudez, L. Mazza, M. Rizzi, N. Goldman, M. Lewenstein, and M. A. Martin-Delgado, Phys. Rev. Lett. **105**, 190404 (2010).
[21] Y.-F. Zhou, H. Jiang, X. C. Xie, and Q.-F. Sun, Phys. Rev. B **95**, 245137 (2017).
[22] B. Svetitsky, S. D. Drell, H. R. Quinn, and M. Weinstein, Phys. Rev. D **22**, 490 (1980).
[23] H. R. Quinn and M. Weinstein, Phys. Rev. Lett. **57**, 2617 (1986).
[24] J. P. Costella, arXiv:hep-lat/0207008; arXiv:hep-lat/0207015.
[25] D. B. Kaplan, Phys. Lett. B **288**, 342 (1992).
[26] D. B. Kaplan and S. Sun, Phys. Rev. Lett. **108**, 181807 (2012).
[27] M. Creutz, arXiv:hep-lat/9410008; Nucl. Phys. B **42**, 56 (1995).
[28] M. Creutz and I. Horvath, Nucl. Phys. B **34**, 583 (1994).
[29] H. B. Nielsen and M. Ninomiya, Phys. Lett. B **105**, 219 (1981); Nucl. Phys. B **185**, 20 (1981).
[30] L. H. Karsten, Phys. Lett. B **104**, 315 (1981).
[31] O. Klein, Z. Phys. **53**, 157 (1929).
[32] M. Katsnelson, K. Novoselov, and A. Geim, Nat. Phys. **2**, 620 (2006).
[33] M. V. Berry and R. J. Mondragon, Proc. R. Soc. London, Ser. A **412**, 53 (1987).
[34] V. Alonso, S. D. Vincenzo, and L. Mondino, Eur. J. Phys. **18**, 315 (1997).
[35] E. McCann and V. I. Fal'ko, J. Phys.: Condens. Matter **16**, 2371 (2004).
[36] C. Ertler, M. Raith, and J. Fabian, Phys. Rev. B **89**, 075432 (2014).
[37] G. J. Ferreira and D. Loss, Phys. Rev. Lett. **111**, 106802 (2013).
[38] A. L. Yeats, P. J. Mintun, Y. Pan, A. Richardella, B. B. Buckley, N. Samarth, and D. D. Awschalom, Proc. Natl. Acad. Sci. USA **114**, 10379 (2017).
[39] G. J. Ferreira, M. N. Leuenberger, D. Loss, and J. C. Egues, Phys. Rev. B **84**, 125453 (2011).
[40] H. Zhang, C.-X. Liu, X.-L. Qi, X. Dai, Z. Fang, and S.-C. Zhang, Nat. Phys. **5**, 438 (2009).
[41] W.-Y. Shan, H.-Z. Lu, and S.-Q. Shen, New J. Phys. **12**, 043048 (2010).
[42] G. Kresse and J. Furthmüller, Comput. Mater. Sci. **6**, 15 (1996).
[43] See Supplemental Material at http://link.aps.org/supplemental/10.1103/PhysRevB.96.161113 for additional details, which includes Refs. [58, 59, 60, 61, 62, 63].
[44] C. W. Groth, M. Wimmer, A. R. Akhmerov, and X. Waintal, New J. Phys. **16**, 063065 (2014).
[45] T. Förster, P. Krüger, and M. Rohlfing, Phys. Rev. B **92**, 201404 (2015).
[46] Y. Zhang, K. He, C.-Z. Chang, C.-L. Song, L.-L. Wang, X. Chen, J.-F. Jia, Z. Fang, X. Dai, W.-Y. Shan, S.-Q. Shen, Q. Niu, X.-L. Qi, S.-C. Zhang, X.-C. Ma, and Q.-K. Xue, Nat. Phys. **6**, 584 (2010).
[47] A. Altland and M. R. Zirnbauer, Phys. Rev. B **55**, 1142 (1997).
[48] D. Bernard and A. LeClair, J. Phys. A **35**, 2555 (2002).
[49] A. P. Schnyder, S. Ryu, A. Furusaki, and A. W. W. Ludwig, Phys. Rev. B **78**, 195125 (2008).
[50] S. Cho, R. Zhong, J. A. Schneeloch, G. Gu, and N. Mason, Sci. Rep. **6**, 21767 (2016).
[51] I. S. S. de Oliveira, W. L. Scopel, and R. H. Miwa, J. Phys.: Condens. Matter **29**, 045302 (2017).
[52] K. Nakada, M. Fujita, G. Dresselhaus, and M. S. Dresselhaus, Phys. Rev. B **54**, 17954 (1996).
[53] L. Brey and H. A. Fertig, Phys. Rev. B **73**, 195408 (2006).
[54] L. Brey and H. A. Fertig, Phys. Rev. B **73**, 235411 (2006).
[55] A. H. Castro Neto, F. Guinea, N. M. R. Peres, K. S. Novoselov, and A. K. Geim, Rev. Mod. Phys. **81**, 109 (2009).
[56] B. A. Bernevig, T. L. Hughes, and S.-C. Zhang, Science **314**, 1757 (2006).
[57] P. Michetti, P. Penteado, J. C. Egues, and P. Recher, Semicond. Sci. Technol. **27**, 124007 (2012).
[58] J. P. Perdew, K. Burke, and M. Ernzerhof, Phys. Rev. Lett. **77**, 3865 (1996).
[59] H. J. Monkhorst and J. D. Pack, Phys. Rev. B **13**, 5188 (1976).
[60] P. E. Blöchl, Phys. Rev. B **50**, 17953 (1994).
[61] K. Lee, E. D. Murray, L. Kong, B. I. Lundqvist, and D. C. Langreth, Phys. Rev. B **82**, 081101 (2010).
[62] Z.-G. Mei, S.-L. Shang, Y. Wang, and Z.-K. Liu, Phys. Rev. B **80**, 104116 (2009).
[63] E. Zhao, C. Zhang, and M. Lababidi, Phys. Rev. B **82**, 205331 (2010).